Title: Structural basis of synergistic neutralization of Crimean-Congo hemorrhagic fever virus by human antibodies

Authors: Akaash K. Mishra[1†], Jan Hellert[2‡†], Natalia Freitas[3], Pablo Guardado-Calvo[2], Ahmed Haouz[4], J. Maximilian Fels[5,#], Daniel P. Maurer[6], Dafna M. Abelson[7], Zachary A. Bornholdt[7], Laura M. Walker[6], Kartik Chandran[5], François-Loïc Cosset[3], Jason S. McLellan[1*], Felix A. Rey[2*]

Affiliations:

[1] Department of Molecular Biosciences, The University of Texas at Austin, Austin, Texas, USA 78712

[2] Structural Virology Unit, Institut Pasteur, CNRS UMR 3569, 25-28 rue du Docteur Roux, Cedex 15, Paris, France 75724

[3] CIRI-Centre International de Recherche en Infectiologie, Univ Lyon, Université Claude Bernard Lyon 1, Inserm, U1111, CNRS, UMR5308, ENS Lyon, 46 allée d'Italie, Lyon, France 69007

[4] Crystallography Platform C2RT, Institut Pasteur, CNRS UMR 3528, 25-28 rue du Docteur Roux, Cedex 15, Paris, France 75724

[5] Department of Microbiology and Immunology, Albert Einstein College of Medicine, Bronx, New York, USA 10461

[6] Adimab LLC, Lebanon, New Hampshire, USA 03766

[7] Mapp Biopharmaceutical Inc., San Diego, California, USA 92121

[‡] Present address: Centre for Structural Systems Biology, Leibniz-Institut für Experimentelle Virologie (HPI), Notkestraße 85, 22607 Hamburg, Germany

[#] Present address: Department of Cell Biology, Harvard Medical School, Boston, Massachusetts, USA; Department of Microbiology, Harvard Medical School, Boston, Massachusetts, USA; Department of Cancer Immunology and Virology, Dana-Farber Cancer Institute, Boston, Massachusetts, USA

†These authors contributed equally

*Correspondence: jmclellan@austin.utexas.edu (J.S.M.); felix.rey@pasteur.fr (F.A.R)

Abstract:

Crimean-Congo hemorrhagic fever virus (CCHFV) is the most widespread tick-borne zoonotic virus, with a 30% case fatality rate in humans. Structural information on the CCHFV membrane fusion glycoprotein Gc–the main target of the host neutralizing antibody response–and on antibody-mediated neutralization mechanisms are lacking. Here we describe the structure of pre-fusion Gc bound to the antigen-binding fragments of two neutralizing antibodies displaying synergy when combined, as well as the structure of trimeric, post-fusion Gc. The structures show the two Fabs acting in concert to block membrane fusion: one targeting the fusion loops and the other blocking Gc trimer formation. The structures also revealed the neutralization mechanism of previously reported anti-CCHFV antibodies, providing the molecular underpinnings essential for developing CCHFV-specific medical countermeasures for epidemic preparedness.

One-Sentence Summary:

The elucidation of antibody neutralization mechanisms of a highly pathogenic virus provides a foundation for epidemic preparedness.

Main Text:

Crimean-Congo hemorrhagic fever virus (CCHFV) is endemic in Africa, Asia and Europe, and is transmitted by ticks and through contact with bodily fluids from viremic animals or patients (*1, 2*). Although infection is asymptomatic in most vertebrates, it can cause severe disease in humans with hemorrhage, myalgia and high fever that eventually leads to death in about 30% of diagnosed cases (*1, 3, 4*). As a result the WHO has shortlisted CCHFV as a priority pathogen in its research and development blueprint (*5*). The highest burden lies on the Balkan peninsula and Turkey, yet global warming facilitates the spread of the tick vector into new habitats carried by migratory birds, as exemplified by a recent outbreak in Spain and by the appearance of infected ticks in Italy (*6-8*).

CCHFV is a member of the *Orthonairovirus* genus in the *Nairoviridae* family of the *Bunyavirales* order of viruses with a segmented, negative-strand RNA genome (*9*). New human pathogens in the *Orthonairovirus* genus (termed nairoviruses from here on) continue to be identified (*10*), highlighting the need for high-resolution structural information to guide antiviral strategies. The *Bunyavirales* order also includes other pathogenic arthropod-borne viruses (or "arboviruses"), such as the Rift Valley fever virus (RVFV, *Phlebovirus* genus, *Phenuiviridae* family), as well as rodent-borne viruses such as Andes virus (*Orthohantavirus* genus, *Hantaviridae* family). CCHFV infects host cells through its envelope glycoproteins Gn and Gc, which form a locally ordered lattice of heterodimers on the virus surface after they are cleaved from a poly-glycoprotein precursor by host proteases (Fig. 1A) (*11-13*). Entry into target cells takes place by receptor-mediated endocytosis (*14*), with the acidic environment of the endosome triggering dissociation of the Gn/Gc heterodimer and the surface lattice, followed by a conformational change of Gc into a trimer of hairpins to drive membrane fusion (Fig. 1B). As for most bunyaviruses, CCHFV Gc is predicted to be a class II membrane fusion protein (*11, 12*) and is the only known target of CCHFV-neutralizing antibodies (*15*).

We determined the X-ray structure of the CCHFV Gc post-fusion trimer using two constructs at resolutions of 2.2 Å and 3.0 Å (Table S1), as described in Materials and Methods. The trimer revealed a typical class II fold, with each protomer adopting the characteristic post-fusion hairpin conformation (*16*). The inner arm of this hairpin is composed of domains I and II, (red and yellow, respectively, in Fig. 1C) and forms a rod-like structure with the distal tip of domain II exposing loops *bc*, *cd* and *ij*, also termed "fusion loops" as they form a non-polar host-membrane insertion surface (HMIS) required to drive membrane fusion. The domain I/II rods make interactions about the 3-fold molecular axis along their entire length to make an elongated trimeric core. The outer arm of the hairpin is formed by domain III (blue) followed by the stem (magenta) running in an extended conformation to reach the HMIS, thus completing the hairpin by bringing the downstream C-terminal trans-membrane segment, which is not included in our structure, next to the HMIS. The turn of the hairpin at the opposite end of the rod is made of a linker region connecting domains I and III (cyan in Fig. 1C). Domain III and the stem together fill the cleft between two neighboring subunits of the core trimer, contributing to the stability of the post-fusion conformation of Gc. The overall arrangement of domains I and III is similar to fusion proteins of other arboviruses such as phleboviruses (*17, 18*), flaviviruses (*19, 20*) and alphaviruses (*21*). This organization is different, however, in hantaviruses (*22, 23*) and in rubella virus (*24*), which do not infect arthropods. In the class II fusion proteins of these mammal-specific viruses, domain III is exchanged between neighboring protomers in the trimer (Fig. S1).

Among the most potently neutralizing human monoclonal antibodies (Mabs) targeting CCHFV Gc, ADI-36121 and ADI-37801 were synergistic in co-neutralization experiments (*15*). We determined the X-ray structure of both Fabs in ternary complex with monomeric Gc to 2.1 Å resolution (Table S1) as described in Materials and Methods. The structure showed a Gc monomer with the ADI-36121 Fab bound at the domain II base and the ADI-37801 Fab

bound at the HMIS (Fig. 1D). The crystals provided interpretable electron density only for domains I, II and part of the domain I/III linker, indicating that the whole outer arm observed in the post-fusion hairpin is mobile in the monomer. On the virion surface, however, the pre-fusion conformation of Gc is likely further stabilized by contacts with Gn and neighboring Gn/Gc heterodimers. Compared to the Gc post-fusion trimer, the conformation of domain I in the monomer is different. In particular, the N- and C-terminal β-strands, A_0 and J_0, display an altered topology (Fig. S1A). A similar change in the conformation of domain I has been observed between the pre- and post-fusion structures of phlebovirus Gc (*17, 18, 25*) (Fig. S1B), indicating that the conformation of domain I in the CCHFV Gc monomer indeed corresponds to the pre-fusion form.

Unlike domain I, the conformation of the domain II tip in the Fab-bound monomer is similar to that seen in the post-fusion trimer (Fig. 2A). In the flavivirus, alphavirus and phlebovirus class II fusion proteins, the HMIS is formed essentially by the *cd* loop alone (orange in our figures) (*16*). In hantaviruses, however, the HMIS is tri-partite, with additional contributions from two adjacent loops, *bc* and *ij* (Fig. 2B) (*22*). CCHFV Gc has a similar tri-partite configuration at its domain II tip, sharing with hantavirus Gc a pattern of conserved residues (Fig. 2C) despite an overall sequence identity of only about 20% between the two Gc orthologs. Fig. 2 compares CCHFV Gc to Maporal virus (MPRLV) Gc, for which the best-resolved pre- and post-fusion hantavirus Gc structures are available (*22, 23, 26*). The main chain conformation of the *bc*, *cd* and *ij* loops is similar in the post-fusion forms of the CCHFV and MPRLV Gc (Fig. 2A and 2B, left panels), with a root-mean-square deviation (RMSD) of 0.8 Å over 29 Cα atom pairs. In both cases, four conserved disulfide bonds (green in Fig. 2A–C) stabilize the structure, two of which cross-link the *cd* loop with the *ij* and *bc* loops (Fig. 2C). In CCHFV, the HMIS conformation is further supported by a hydrogen bond network that involves the buried polar side chains of Asn1194 and Arg1189 of the *cd* loop in both the pre-

and post-fusion forms (Fig. 2A–C). The equivalent residues in MPRLV, Asn769 and Asn764, recapitulate the same interactions in the post-fusion form *(26)* but are solvent-exposed in the pre-fusion Gn/Gc heterodimer, where non-polar side chains such as MPRLV Trp766, corresponding to CCHFV Trp1191, are buried instead (Fig. 2B). It is likely that Gn locks the domain II tip in the conformation shown in the MPRLV pre-fusion Gn/Gc complex and that release of Gn results in the HMIS conformation seen in the pre and post-fusion forms of CCHFV. This suggests that the Gc monomer observed in the ternary complex corresponds to an activated pre-fusion form of CCHFV capable of insertion into the host membrane.

To experimentally test the role of residues suggested by the structure to be important for Gc function in membrane fusion, we established an assay to follow syncytia formation of cells expressing the CCHFV glycoproteins at their surface upon low pH treatment. We used this assay to test single point mutations at the interface between domains I and III (at the turn of the post-fusion hairpin) to explore their functional impact. Alanine substitutions of two conserved residues, His1479 on domain III, which makes a salt bridge with Glu1113 of domain I, and Trp1068 in the N-terminal tail, which projects into a pocket at the domain I/II boundary, abrogated low pH-triggered cell-cell fusion (Fig. 2D-E). Gc-derived linear peptides spanning the N-terminal tail (aa 1041–1060 & 1061–1080) around the functionally important Trp1068 residue robustly react with CCHFV-positive human sera *(27)*, suggesting this site as a potential target for neutralizing antibodies. On the contrary, we saw no effect by alanine substitution of His1398 at the binding pocket for the N-terminal tail, and only a mild effect by alanine substitution of the glycosylation site Asn1563 on the stem (*28*) (Fig. 2D-E).

We also tested the role of nonpolar side chains of the HMIS. Mutation to alanine of the highly conserved Trp1191, Trp1197 and Trp1199 exposed by the *cd* loop, as well as Trp1365 and Met1362 exposed by the *ij* loop (see Fig. 2C), strongly impaired low pH-triggered syncytia formation relative to wild type Gc when substituted individually (Fig. 2D). This result is in line

with the functional effect of the corresponding residues of hantavirus Gc (Fig. 2B), which had been also shown to be functionally required for target membrane insertion (*22*).

The residues exposed at the HMIS constitute the epitope of Mab ADI-37801, which covers 627 Å^2 of surface area on Gc. Two thirds of the epitope are buried by the three complementarity-determining regions (CDRs) H1, H2 and H3 of the heavy chain, and the remainder by the light chain CDRs L1 and L3 (Fig. 2F). There are four hydrogen bonds at the epitope/paratope interface (Table S2). The core of the epitope is formed by the *cd* loop, which contributes ten amino acids, whereas the *bc* loop contributes an additional two. The residues critical for membrane fusion—Trp1191, Trp1197 and Trp1199 of the *cd* loop—are an integral part of the ADI-37801 epitope (Fig. 2A and 2F). Our structure is thus consistent with the yeast-display-based epitope mapping, which identified Trp1199 as critical for ADI-37801 binding (*15*).

Our crystals of the ternary complex grew at pH 5.6, suggesting that the complex of Gc and ADI-37801 remains stable in the endosome during viral entry. Using biolayer interferometry (BLI), we confirmed that ADI-37801 binding is insensitive to mildly acidic conditions (Fig. 2G). Taken together, the cell-cell fusion, structural and kinetic data suggest that ADI-37801 inhibits endosomal membrane insertion of Gc by masking its fusion loops.

The X-ray structure showed that ADI-36121 binds laterally to the domain II base adjacent to the Asn1345 glycan and covers 943 Å^2 of surface area on Gc, 63% and 37% of which are buried by the heavy and light chains, respectively, involving all six CDRs (Fig. 3A-B). The epitope is composed of 22 residues featuring 13 hydrogen bonds and one salt bridge at the interface (Table S2). The structure is consistent with the yeast-display-based mutagenesis screen that identified Leu1307 and Ile1229 as important for ADI-36121 binding (Fig. 3B) (*15*).

Structural comparison shows that the ADI-36121 epitope becomes entirely buried at the trimer interface upon formation of the post-fusion trimer of Gc (Fig. 3C-D). To experimentally

confirm that the ADI-36121 epitope is inaccessible in the post-fusion trimer, we used BLI to compare antibody binding to both monomeric and trimeric fractions of recombinant soluble Gc. The affinity of ADI-36121 was approximately 200-fold higher for the monomeric fraction than for the trimeric fraction (Fig. 3E). The observed residual ADI-36121 binding to the trimeric fraction suggests contamination of the sample with Gc monomers, as trimeric and monomeric fractions eluted in partially overlapping peaks in size-exclusion chromatography (Fig. S2). Nevertheless, antibody binding likely outcompetes the trimerization process during viral infection, since the K_D of ADI-36121 for the Gc monomer is in the picomolar range at pH 7.5 and 5.5 (Fig. 3F). These data suggest that ADI-36121 neutralizes CCHFV by blocking Gc homotrimerization in the endosome and preventing membrane fusion.

The CCHFV-neutralizing human antibodies described previously had been tentatively assigned to six different antigenic sites using a homology model for Gc based on the MPRLV Gc structure (*15*). Our experimental structures confirm the proposed distribution of the epitopes among the three Gc domains, and they now also reveal the neutralization mechanisms by showing that they map to the HMIS or other surfaces that become buried during Gc-driven membrane fusion (Fig. 4A). The dominant antigenic site 1 maps to the *cd* loop (Fig. 4A), which is conserved across CCHFV strains as well as across members of the *Orthonairovirus* genus (Fig. 4B-C, S3 and S4). Antigenic sites 2–4 map to the domain II base, with sites 2 and 3 at the trimer core interface of post-fusion Gc (Fig. 4A). The most potently neutralizing antibodies, including ADI-36121, target site 3. Consistent with the high degree of conservation of its epitope across CCHFV strains (Fig. 4B), ADI-36121 displays highly potent cross-clade neutralization (*15*), which makes it a viable candidate for clinical development. It remains to be investigated whether this Mab would be effective against nairoviruses from other serogroups, such as the veterinary pathogens Dugbe virus or Nairobi sheep disease virus - which can potentially spillover to humans (*29*), as Gc from these viruses carries several point

mutations in the epitope (Fig. S4 and S5). Site 4 maps to the opposite face of domain II, near the interface with domain III and the stem in the post-fusion structure (Fig. 4A), suggesting that antibody binding would inhibit hairpin formation. Similar to sites 2 and 3, site 5 overlaps with the Gc trimer interface but lies within domain I (Fig. 4A). Moreover, antibody binding to site 5 likely restrains the conformational change of domain I during fusion (Fig. S1A). Finally, site 6 maps to domain III, where antibody binding may sterically inhibit its translocation for post-fusion hairpin formation (Fig. 4A). In addition to human antibodies, this site is likely also targeted by the broadly neutralizing murine antibody 11E7, which has been mapped to a Gc fragment encompassing both domain III and the stem (aa 1443–1566) (*30*). As the epitope was sensitive to chemical reduction, it can now be assigned to the disulfide-stabilized domain III. Because domain III contains more sequence polymorphisms across CCHFV strains than the other Gc domains (Fig. 4B), cross-clade neutralization by site 6 antibodies may be more limited compared to the other sites. While inhibition of binding to the yet unknown entry receptor for CCHFV may also play a role in neutralization, our findings are consistent with a neutralization mechanism that inhibits membrane fusion, either by blocking insertion of the HMIS into target membranes, by interfering with Gc trimerization, or by inhibiting post-fusion hairpin formation.

Our structural data revealed that the HMIS of CCHFV Gc is at least transiently accessible on virus particles, as Mab ADI-37801 efficiently neutralizes the virus. Yet the current paradigm is that the HMIS is protected by the companion protein Gn from premature exposure. The only available high-resolution structures of a bunyavirus Gn/Gc complex come from hantaviruses, and indeed they show that the conformation of the Gc domain II tip in interaction with Gn is such that the HMIS is not formed. Recent studies on Andes hantavirus have however shown a significant degree of breathing, transiently exposing the HMIS at physiological temperatures (*31*). The strong structural similarity between their domain II tips (Fig. 2A and 2C) suggest that comparable breathing dynamics can also be expected from

CCHFV Gc. Since ADI-37801 neutralization was strain-dependent (*15*) despite almost perfect conservation of the HMIS sequence across CCHFV strains (Fig. S3), the breathing dynamics of the HMIS are likely controlled by sequences outside the fusion loops. Of note, strain-dependent breathing is also known to affect the neutralization potency of fusion loop antibodies in flaviviruses (*32, 33*).

Unlike the fusion loop antibody ADI-37801, the trimerization-inhibiting antibody ADI-36121 showed potent neutralization across CCHFV strains (*15*), indicating that accessibility of its epitope is not restricted by strain-dependent structural dynamics within the envelope. The ADI-36121 epitope on CCHFV Gc lies in the same position as the P-4G2 epitope on hantavirus Gc (Fig. S6). Both antibodies bind to the same secondary structure elements on their respective Gc targets (Fig. S6C), at a surface patch that is involved in lateral inter-spike contacts on the hantavirus glycoprotein lattice (Figs. S6A and S6D). This surface patch becomes buried in the Gc post-fusion trimer in both cases. Low resolution studies of Hazara virus, a non-pathogenic nairovirus, showed tetrameric spikes arranged in a square surface lattice (*34*), similar to that of hantaviruses, which was visualized at higher resolution (*26*) and which is very different from the icosahedral T=12 Gn/Gc lattice of the phlebovirus RVFV, for which relatively high-resolution structures are available (*35*). Considering the similar square surface lattices of nairo- and hantaviruses, and the structural similarity between the corresponding fusion proteins, it is reasonable to expect that comparable surfaces in CCHFV Gc are involved in lateral spike-spike contacts (see Figs. S6B and S6E). It is possible therefore that ADI-36121 perturbs the long-range order of the CCHFV envelope in a similar way as was shown for P-4G2 (*36*). Higher-resolution cryo-electron tomography data on the nairovirus surface glycoprotein lattice are needed to identify the precise lateral spike-spike contacts and confirm the predictions illustrated in Fig. S6. Our study nevertheless raises important parallels between these two zoonotic viruses, despite their different life-styles and reservoirs - one of them being arthropod-borne and the

other being transmitted by small mammals - highlighting the power of comparative structural studies to understand common features of emerging viruses.

The combination of antibodies ADI-37801 and ADI-36121 displayed synergy in a neutralization assay (*15*). Moreover, a single dose of a bispecific antibody containing the variable domains of both ADI-36121 and ADI-37801 protected mice against CCHFV even when administered 24 h post-exposure, while the individual Mabs protected only in a prophylactic setting (*15*). To explain these findings, our structural analysis suggests that ADI-36121 binding indirectly influences the Gc fusion loop breathing dynamics by perturbation of the glycoprotein surface lattice in such a way that the HMIS becomes more exposed, allowing ADI-37801 to recognize its epitope more easily (Fig. S6E-F). Combination with ADI-36121 should therefore also broaden the reactivity of ADI-37801 with the various CCHFV strains, making these two antibodies strong candidates for therapeutic antibody cocktails. Describing CCHFV neutralization at the mechanistic level, our data guide the design of future therapeutic antibodies and will likewise support the design of protective CCHFV vaccines.

References and Notes

1. O. Ergonul, Crimean-Congo haemorrhagic fever. *Lancet Infect Dis* **6**, 203-214 (2006).
2. K. Tsergouli, T. Karampatakis, A. B. Haidich, S. Metallidis, A. Papa, Nosocomial infections caused by Crimean-Congo haemorrhagic fever virus. *J Hosp Infect* **105**, 43-52 (2020).
3. E. Akinci, H. Bodur, H. Leblebicioglu, Pathogenesis of Crimean-Congo hemorrhagic fever. *Vector Borne Zoonotic Dis* **13**, 429-437 (2013).
4. D. A. Bente *et al.*, Crimean-Congo hemorrhagic fever: history, epidemiology, pathogenesis, clinical syndrome and genetic diversity. *Antiviral Res* **100**, 159-189 (2013).
5. M. S. Mehand, F. Al-Shorbaji, P. Millett, B. Murgue, The WHO R&D Blueprint: 2018 review of emerging infectious diseases requiring urgent research and development efforts. *Antiviral Res* **159**, 63-67 (2018).
6. E. Mancuso *et al.*, Crimean-Congo Hemorrhagic Fever Virus Genome in Tick from Migratory Bird, Italy. *Emerg Infect Dis* **25**, 1418-1420 (2019).
7. A. Negredo *et al.*, Autochthonous Crimean-Congo Hemorrhagic Fever in Spain. *N Engl J Med* **377**, 154-161 (2017).
8. A. Negredo *et al.*, Survey of Crimean-Congo Hemorrhagic Fever Enzootic Focus, Spain, 2011-2015. *Emerg Infect Dis* **25**, 1177-1184 (2019).
9. P. Maes *et al.*, Taxonomy of the order Bunyavirales: second update 2018. *Arch Virol* **164**, 927-941 (2019).
10. J. Ma *et al.*, Identification of a new orthonairovirus associated with human febrile illness in China. *Nat Med* **27**, 434-439 (2021).
11. P. Guardado-Calvo, F. A. Rey, The Envelope Proteins of the Bunyavirales. *Adv Virus Res* **98**, 83-118 (2017).
12. R. J. G. Hulswit, G. C. Paesen, T. A. Bowden, X. Shi, Recent Advances in Bunyavirus Glycoprotein Research: Precursor Processing, Receptor Binding and Structure. *Viruses* **13**, (2021).
13. M. J. Vincent *et al.*, Crimean-Congo hemorrhagic fever virus glycoprotein proteolytic processing by subtilase SKI-1. *J Virol* **77**, 8640-8649 (2003).
14. A. Albornoz, A. B. Hoffmann, P.-Y. Lozach, N. D. Tischler, Early Bunyavirus-Host Cell Interactions. *Viruses* **8**, 143 (2016).
15. J. M. Fels *et al.*, Protective neutralizing antibodies from human survivors of Crimean-Congo hemorrhagic fever. *Cell*, (2021).
16. Y. Modis, Class II fusion proteins. *Adv Exp Med Biol* **790**, 150-166 (2013).
17. P. Guardado-Calvo *et al.*, A glycerophospholipid-specific pocket in the RVFV class II fusion protein drives target membrane insertion. *Science* **358**, 663-667 (2017).
18. S. Halldorsson *et al.*, Structure of a phleboviral envelope glycoprotein reveals a consolidated model of membrane fusion. *Proc Natl Acad Sci U S A* **113**, 7154-7159 (2016).
19. S. Bressanelli *et al.*, Structure of a flavivirus envelope glycoprotein in its low-pH-induced membrane fusion conformation. *EMBO J* **23**, 728-738 (2004).
20. Y. Modis, S. Ogata, D. Clements, S. C. Harrison, Structure of the dengue virus envelope protein after membrane fusion. *Nature* **427**, 313-319 (2004).
21. D. L. Gibbons *et al.*, Conformational change and protein-protein interactions of the fusion protein of Semliki Forest virus. *Nature* **427**, 320-325 (2004).

22. P. Guardado-Calvo *et al.*, Mechanistic Insight into Bunyavirus-Induced Membrane Fusion from Structure-Function Analyses of the Hantavirus Envelope Glycoprotein Gc. *PLoS Pathog* **12**, e1005813 (2016).
23. S. Willensky *et al.*, Crystal Structure of Glycoprotein C from a Hantavirus in the Post-fusion Conformation. *PLoS Pathog* **12**, e1005948 (2016).
24. R. M. DuBois *et al.*, Functional and evolutionary insight from the crystal structure of rubella virus protein E1. *Nature* **493**, 552-556 (2013).
25. M. Dessau, Y. Modis, Crystal structure of glycoprotein C from Rift Valley fever virus. *Proc Natl Acad Sci U S A* **110**, 1696-1701 (2013).
26. A. Serris *et al.*, The Hantavirus Surface Glycoprotein Lattice and Its Fusion Control Mechanism. *Cell* **183**, 442-456 e416 (2020).
27. A. Fritzen *et al.*, Epitope-mapping of the glycoprotein from Crimean-Congo hemorrhagic fever virus using a microarray approach. *PLoS Negl Trop Dis* **12**, e0006598 (2018).
28. B. R. Erickson, V. Deyde, A. J. Sanchez, M. J. Vincent, S. T. Nichol, N-linked glycosylation of Gn (but not Gc) is important for Crimean Congo hemorrhagic fever virus glycoprotein localization and transport. *Virology* **361**, 348-355 (2007).
29. in *Fenner's Veterinary Virology (Fifth Edition),* N. J. MacLachlan, E. J. Dubovi, Eds. (Academic Press, Boston, 2017), pp. 411-424.
30. A. A. Ahmed *et al.*, Presence of broadly reactive and group-specific neutralizing epitopes on newly described isolates of Crimean-Congo hemorrhagic fever virus. *J Gen Virol* **86**, 3327-3336 (2005).
31. E. A. Bignon, A. Albornoz, P. Guardado-Calvo, F. A. Rey, N. D. Tischler, Molecular organization and dynamics of the fusion protein Gc at the hantavirus surface. *Elife* **8**, (2019).
32. K. A. Dowd, T. C. Pierson, The Many Faces of a Dynamic Virion: Implications of Viral Breathing on Flavivirus Biology and Immunogenicity. *Annu Rev Virol* **5**, 185-207 (2018).
33. F. A. Rey, K. Stiasny, M. C. Vaney, M. Dellarole, F. X. Heinz, The bright and the dark side of human antibody responses to flaviviruses: lessons for vaccine design. *EMBO Rep* **19**, 206-224 (2018).
34. E. K. Punch *et al.*, Potassium is a trigger for conformational change in the fusion spike of an enveloped RNA virus. *J Biol Chem* **293**, 9937-9944 (2018).
35. S. Halldorsson *et al.*, Shielding and activation of a viral membrane fusion protein. *Nat Commun* **9**, 349 (2018).
36. I. Rissanen *et al.*, Molecular rationale for antibody-mediated targeting of the hantavirus fusion glycoprotein. *Elife* **9**, (2020).
37. E. Bergeron, M. J. Vincent, S. T. Nichol, Crimean-Congo hemorrhagic fever virus glycoprotein processing by the endoprotease SKI-1/S1P is critical for virus infectivity. *Journal of virology* **81**, 13271-13276 (2007).
38. D. E. Klein, J. L. Choi, S. C. Harrison, Structure of a dengue virus envelope protein late-stage fusion intermediate. *J Virol* **87**, 2287-2293 (2013).
39. T. Iwaki, M. Figuera, V. A. Ploplis, F. J. Castellino, Rapid selection of Drosophila S2 cells with the puromycin resistance gene. *Biotechniques* **35**, 482-484, 486 (2003).
40. P. Weber *et al.*, High-Throughput Crystallization Pipeline at the Crystallography Core Facility of the Institut Pasteur. *Molecules* **24**, (2019).
41. W. Kabsch, Integration, scaling, space-group assignment and post-refinement. *Acta Crystallogr D Biol Crystallogr* **66**, 133-144 (2010).
42. P. R. Evans, G. N. Murshudov, How good are my data and what is the resolution? *Acta Crystallogr D Biol Crystallogr* **69**, 1204-1214 (2013).

43. T. C. Terwilliger *et al.*, Decision-making in structure solution using Bayesian estimates of map quality: the PHENIX AutoSol wizard. *Acta Crystallogr D Biol Crystallogr* **65**, 582-601 (2009).
44. P. Emsley, K. Cowtan, Coot: model-building tools for molecular graphics. *Acta Crystallogr D Biol Crystallogr* **60**, 2126-2132 (2004).
45. P. D. Adams *et al.*, PHENIX: a comprehensive Python-based system for macromolecular structure solution. *Acta Crystallogr D Biol Crystallogr* **66**, 213-221 (2010).
46. M. D. Winn *et al.*, Overview of the CCP4 suite and current developments. *Acta Crystallogr D Biol Crystallogr* **67**, 235-242 (2011).
47. T. G. Battye, L. Kontogiannis, O. Johnson, H. R. Powell, A. G. Leslie, iMOSFLM: a new graphical interface for diffraction-image processing with MOSFLM. *Acta Crystallogr D Biol Crystallogr* **67**, 271-281 (2011).
48. A. J. McCoy *et al.*, Phaser crystallographic software. *J Appl Crystallogr* **40**, 658-674 (2007).
49. G. Chojnowski *et al.*, The use of local structural similarity of distant homologues for crystallographic model building from a molecular-replacement solution. *Acta Crystallogr D Struct Biol* **76**, 248-260 (2020).
50. G. Langer, S. X. Cohen, V. S. Lamzin, A. Perrakis, Automated macromolecular model building for X-ray crystallography using ARP/wARP version 7. *Nat Protoc* **3**, 1171-1179 (2008).
51. G. Bunkoczi, R. J. Read, Improvement of molecular-replacement models with Sculptor. *Acta Crystallogr D Biol Crystallogr* **67**, 303-312 (2011).
52. S. Devignot, E. Bergeron, S. Nichol, A. Mirazimi, F. Weber, A virus-like particle system identifies the endonuclease domain of Crimean-Congo hemorrhagic fever virus. *J Virol* **89**, 5957-5967 (2015).
53. N. Freitas *et al.*, The interplays between Crimean-Congo hemorrhagic fever virus (CCHFV) M segment-encoded accessory proteins and structural proteins promote virus assembly and infectivity. *PLoS Pathog* **16**, e1008850 (2020).
54. D. Lavillette *et al.*, Characterization of fusion determinants points to the involvement of three discrete regions of both E1 and E2 glycoproteins in the membrane fusion process of hepatitis C virus. *J Virol* **81**, 8752-8765 (2007).
55. A. R. Garrison *et al.*, A DNA vaccine for Crimean-Congo hemorrhagic fever protects against disease and death in two lethal mouse models. *PLoS Negl Trop Dis* **11**, e0005908 (2017).
56. G. Wengler, G. Wengler, F. A. Rey, The isolation of the ectodomain of the alphavirus E1 protein as a soluble hemagglutinin and its crystallization. *Virology* **257**, 472-482 (1999).
57. A. Waterhouse *et al.*, SWISS-MODEL: homology modelling of protein structures and complexes. *Nucleic Acids Res* **46**, W296-W303 (2018).

Acknowledgments:

We thank members of the McLellan and Rey laboratories for providing helpful comments on the manuscript; Fabrice Agou from the Chemogenomic and Biological Screening platform at Institut Pasteur; the staff of the Crystallography platform at Institut Pasteur, of the synchrotron

beamlines PX2 at SOLEIL (St Aubin, France), ID23-1 at the ESRF (Grenoble, France) and 19-ID at Argonne that is operated by UChicago Argonne, LLC for the US Department of Energy (DOE), Office of Biological and Environmental Research under Contract DE-AC02-06CH11357.

Funding:

This work was supported by National Institutes of Health award U19 AI142777 to J.S.M., Z.A.B., K.C., L.M.W, as well as by Institut Pasteur, CNRS and grant ANR-10-LABX-62-10 IBEID to F.A.R and by the LabEx Ecofect (ANR-11-LABX-0048) of the "Université de Lyon", within the program "Investissements d'Avenir" (ANR-11-IDEX-0007) operated by the French National Research Agency (ANR), to F.-L.C. Research was funded in part by Welch Foundation grant F-0003-19620604 awarded to J.S.M. The Pasteur-Cantarini fellowship for 24 months was granted to J.H. who was further supported by the Région Ile de France (Domaine d'intérêt majeur - innovative technologies for life sciences, DIM 1HEALTH).

Author contributions

Conceptualization A.K.M., J.H., J.S.M. and F.A.R.; methodology and formal analysis A.K.M., J.H., N.F., P.G.-C., F.-L.C., J.S.M. and F.A.R.; investigation A.K.M., J.H., N.F., P.G.-C. and A.H.; resources J.M.F, D.P.M and D.M.A.; writing A.K.M., J.H., J.S.M. and F.A.R.; reviewing and editing, all authors; visualization J.H., A.K.M., J.S.M. and F.A.R.; supervision F.A.R., J.S.M., F.- L.C., K.C., L.M.W., Z.A.B. and P.G-C.; funding acquisition F.A.R., J.S.M., F.-L.C., K.C., L.M.W., Z.A.B. and J.H.

Competing Interests

F.A.R. is board member and shareholder of *EureKARE* and *MELETIUS Therapeutics*. D.M.A and Z.A.B are employees and shareholders at Mapp Biopharmaceutical, Inc. L.M.W. is an employee at Adimab, LLC; D.P.M. and L.M.W. are shareholders of Adimab, LLC. K.C. has consulted for Axon Advisors, is a member of the scientific advisory boards of Integrum Scientific, LLC and Biovaxys Technology Corp., LLC; K.C. and J.S.M. are members of the scientific advisory board of the Pandemic Security Initiative of Celdara, LLC. A.K.M., J.M.F., D.P.M., D.M.A., Z.A.B., L.M.W., K.C. and J.S.M. are listed as inventors on a pending patent application with provisional number 63/021,004, entitled *Anti-Crimean-Congo Hemorrhagic Fever Virus antibodies, and methods of their generation and use*.

Data and material availability

Atomic coordinates of the reported structures have been deposited in the Protein Data Bank under accession codes 7A59, 7A5A, 7L7R and 7KX4. Antibodies ADI-37801 and ADI-36121 are available from the corresponding author J.S.M. under a material transfer agreement with the University of Texas at Austin.

Supplementary Materials

Materials and Methods
Figs. S1 to S6
Tables S1 to S2

Figure Captions

Fig. 1. Structures of CCHFV Gc. A) Organization of the CCHFV glycoprotein precursor **B)** Mechanism of bunyavirus class II membrane fusion proteins. **C)** X-ray structure of the CCHFV Gc ectodomain in post-fusion conformation. The front protomer is colored by domains and the trimer axis is shown in light blue. Secondary structure elements and disulfide bonds (green numbers) are labeled. An orthonairovirus-specific insertions cluster (IC) is depicted in brown. **D)** X-ray structure of the CCHFV Gc monomer in complex with the ADI-37801 and ADI-36121 Fabs.

Fig. 2. ADI-37801 binds HMIS residues required for Gc driven syncytia formation. A) The CCHFV HMIS of the post-fusion trimer (left) and in complex with ADI-37801 (right). In the left panel, W1191, W1197 and W1199, mutated to obtain the crystals, have been modeled for clarity. **B)** The hantavirus fusion loops in the post-fusion trimer forming the HMIS (left, PDB:6y68, MPRLV structure) and in the pre-fusion Gn/Gc heterodimer, where the HMIS is not formed (right, PDB:6y62) (*15*). **C)** Fusion loop sequences of CCHFV Gc with consensus sequence logo for the *Orthonairovirus* (top) and *Orthohantavirus* (bottom) genera. The bar chart shows the exposed surface area per residue in pre- (hantavirus Gc) and post-fusion (CCHFV and hantavirus Gc) structures. The accessible and buried surface per residue are represented in grey and black, respectively. Non-polar residues are black, acidic red, basic blue and cysteines green. **D)** CCHFV Gc-induced syncytia formation by wild-type and indicated mutant Gc at neutral and acidic pH. The transfected cell surface expression is shown for each mutant below. **E)** Details of two alternative conformations of the N-tail and a pH-sensitive salt bridge between domains I and III. The helical conformation (top) is dominant, whereas the β-hairpin (bottom) is well defined in only two of the six polypeptide chains in the asymmetric unit of the monoclinic crystals obtained at pH 7.5. The view is as in Fig. 1C. **F)** Interface

between the ADI-37801 CDRs and the Gc fusion loops. The antibody heavy and light chain CDRs are respectively colored blue and gray. CCHFV Gc is colored orange (*cd* loop) and yellow (*bc* loop). Polar interactions denoted as dashed lines. **G)** BLI sensorgrams showing binding kinetics of CCHFV Gc^{1579} to ADI-37801 at pH 7.5 (top) or pH 5.5 (bottom).

Fig. 3. ADI-36121 epitope is buried at the trimer interface of the post-fusion hairpin. A) The CCHFV Gc monomer in complex with the ADI-36121 Fab. **B)** The CDRs interacting with the Gc domain II base. Green and gray indicate heavy and light chains, respectively, and yellow indicates Gc domain II. Polar interactions are shown by dashes. **C)** Superposition of the ADI-36121 complex with the Gc post-fusion trimer. The trimer's front protomer is shown in ribbons colored by domains and the flanking protomers as a white surface. **D)** One trimer protomer shown as surface colored by domains with the trimer interface outlined and the ADI-36121 footprint superposed in green, illustrating that the epitope is occluded in the trimer. **E)** BLI sensograms showing binding kinetics of the monomeric fraction (top) or the trimeric fraction (bottom) of CCHFV Gc^{1572} W3 to ADI-36121 at pH 7.5. **F)** BLI sensograms showing binding kinetics of CCHFV Gc^{1579} to ADI-36121 at pH 7.5 (top) or pH 5.5 (bottom). See Materials and Methods for details of the constructs used.

Fig. 4. The epitopes of CCHFV-neutralizing human antibodies map to Gc surfaces involved in driving membrane fusion. A) Antigenic sites mapped on the surface of one CCHFV Gc protomer within the post-fusion trimer. The trimer axis is shown in light blue. Only the front Gc subunit is shown in the right panel, after a 180° rotation about the trimer axis. The trimer interface is outlined in black. **B)** Sequence variability across 15 representative CCHFV strains (Fig. S3) color-plotted on the Gc surface. **C)** Sequence variability across 14 species in the *Orthonairovirus* genus (Fig. S4).

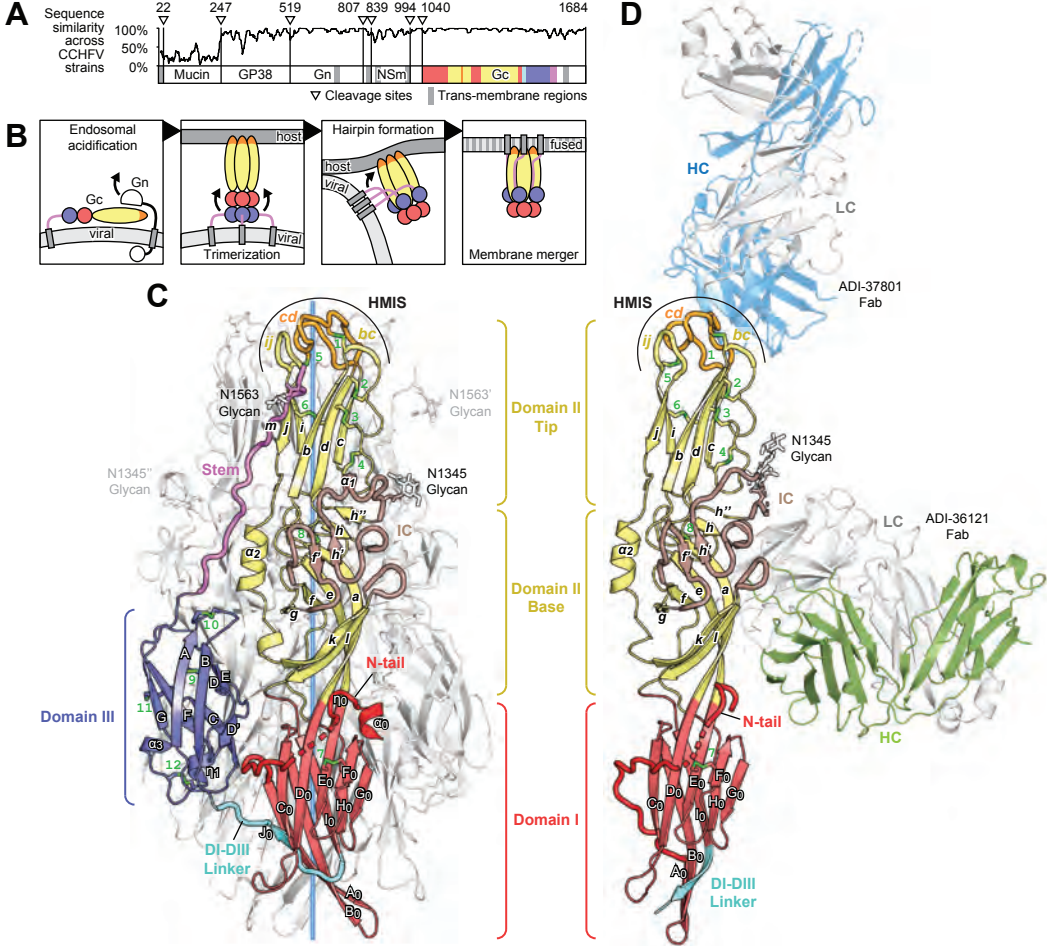
A
Sequence similarity across CCHFV strains
100%
50%
0%
22
247
519
807
839
994
1040
1684
Mucin
GP38
Gn
NSm
Gc
Cleavage sites
Trans-membrane regions
B
Endosomal acidification
Gc
Gn
viral
host
viral
Trimerization
Hairpin formation
host
viral
fused
Membrane merger
C
HMIS
cd
bc
ij
N1563 Glycan
N1563' Glycan
N1345'' Glycan
Stem
N1345 Glycan
IC
N-tail
Domain II Tip
Domain II Base
Domain III
Domain I
DI-DIII Linker
D
HC
LC
ADI-37801 Fab
HMIS
N1345 Glycan
IC
LC
ADI-36121 Fab
HC
N-tail
DI-DIII Linker

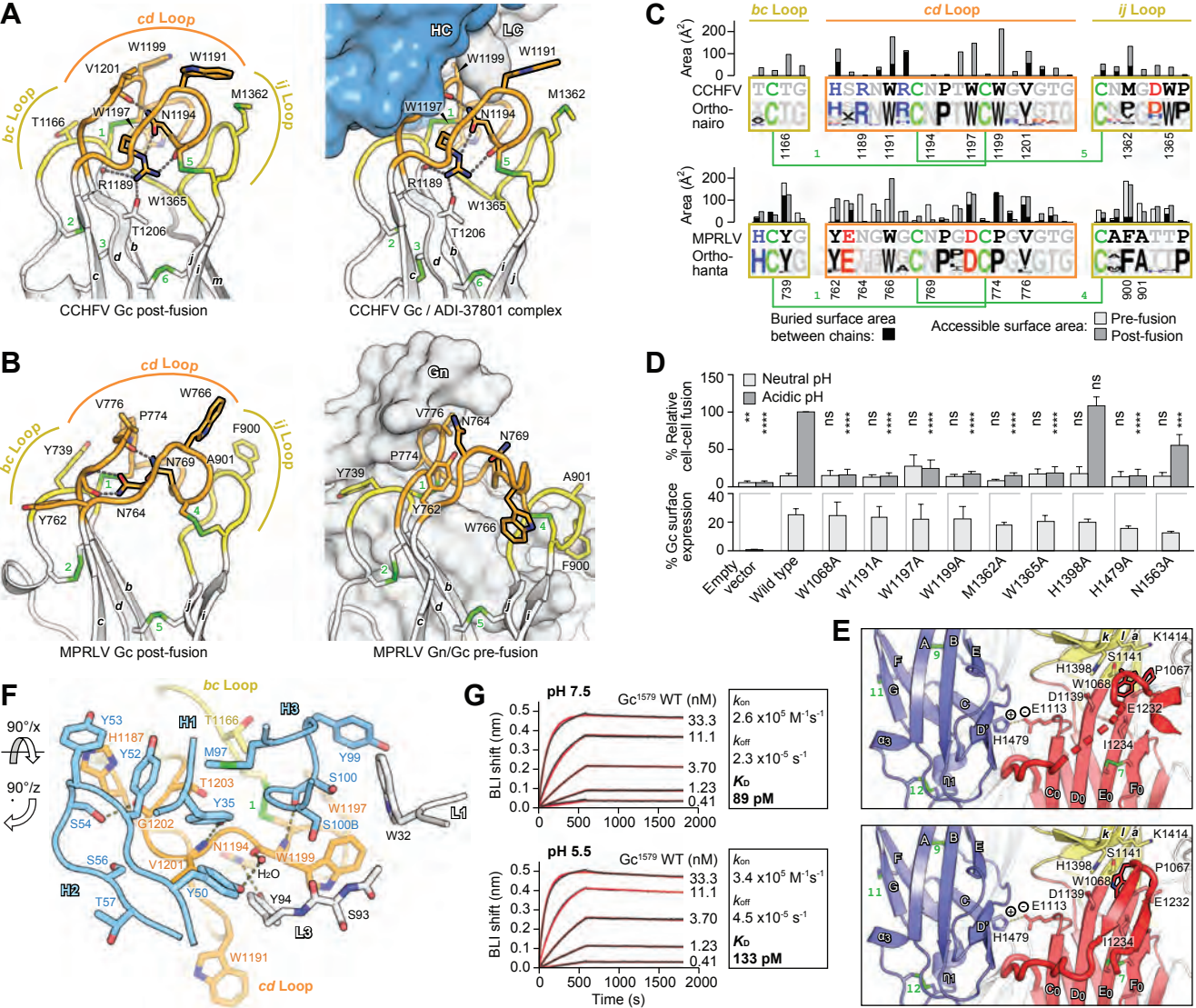
A
cd Loop
bc Loop
ij Loop
W1199
W1191
V1201
M1362
T1166
W1197
N1194
R1189
W1365
T1206
HC
LC
CCHFV Gc post-fusion
CCHFV Gc / ADI-37801 complex
B
V776
W766
P774
F900
Y739
N769
A901
Y762
N764
Gn
MPRLV Gc post-fusion
MPRLV Gn/Gc pre-fusion
C
bc Loop
cd Loop
ij Loop
Area (Å²)
CCHFV Ortho-nairo
MPRLV Ortho-hanta
Buried surface area between chains:
Accessible surface area:
Pre-fusion
Post-fusion
D
Neutral pH
Acidic pH
% Relative cell-cell fusion
% Gc surface expression
Empty vector
Wild type
W1068A
W1191A
W1197A
W1199A
M1362A
W1365A
H1398A
H1479A
N1563A
E
F
bc Loop
H1
H3
L1
W32
H2
L3
cd Loop
90°/x
90°/z
G
pH 7.5
pH 5.5
Gc1579 WT (nM)
BLI shift (nm)
Time (s)
kon
koff
KD
2.6 x10⁵ M⁻¹s⁻¹
2.3 x10⁻⁵ s⁻¹
89 pM
3.4 x10⁵ M⁻¹s⁻¹
4.5 x10⁻⁵ s⁻¹
133 pM

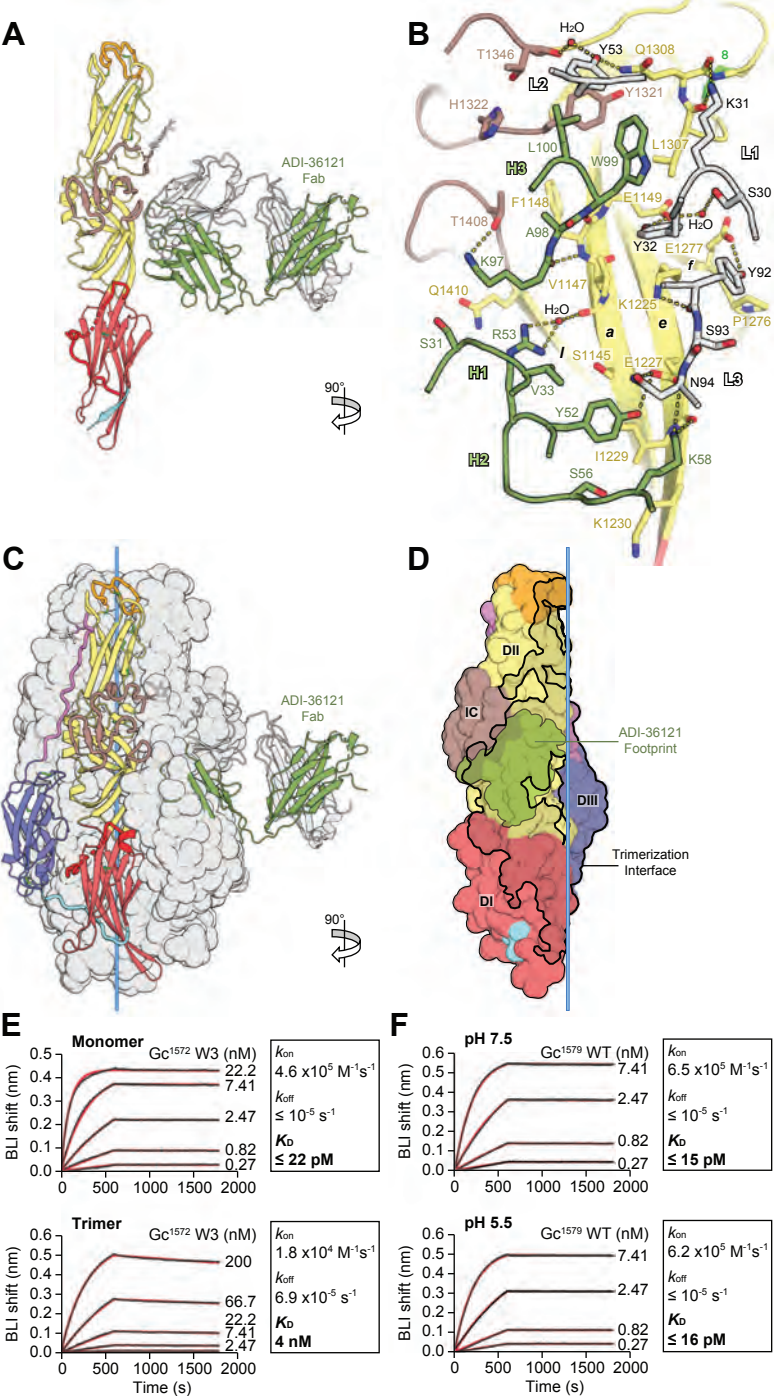
A
ADI-36121
Fab
90°
B
H2O
T1346
Y53
Q1308
8
L2
Y1321
H1322
K31
L100
L1307
L1
H3
W99
S30
F1148
E1149
T1408
H2O
A98
Y32
E1277
K97
f
Y92
Q1410
V1147
H2O
K1225
P1276
R53
a
e
S93
S31
l
S1145
E1227
H1
N94
L3
V33
Y52
I1229
K58
H2
S56
K1230
C
ADI-36121
Fab
90°
D
DII
IC
ADI-36121
Footprint
DIII
Trimerization
Interface
DI
E
Monomer
Gc1572 W3 (nM)
22.2
7.41
2.47
0.82
0.27
kon
4.6 x10^5 M^-1 s^-1
koff
≤ 10^-5 s^-1
KD
≤ 22 pM
BLI shift (nm)
Trimer
Gc1572 W3 (nM)
200
66.7
22.2
7.41
2.47
kon
1.8 x10^4 M^-1 s^-1
koff
6.9 x10^-5 s^-1
KD
4 nM
Time (s)
F
pH 7.5
Gc1579 WT (nM)
7.41
2.47
0.82
0.27
kon
6.5 x10^5 M^-1 s^-1
koff
≤ 10^-5 s^-1
KD
≤ 15 pM
pH 5.5
Gc1579 WT (nM)
7.41
2.47
0.82
0.27
kon
6.2 x10^5 M^-1 s^-1
koff
≤ 10^-5 s^-1
KD
≤ 16 pM
Time (s)

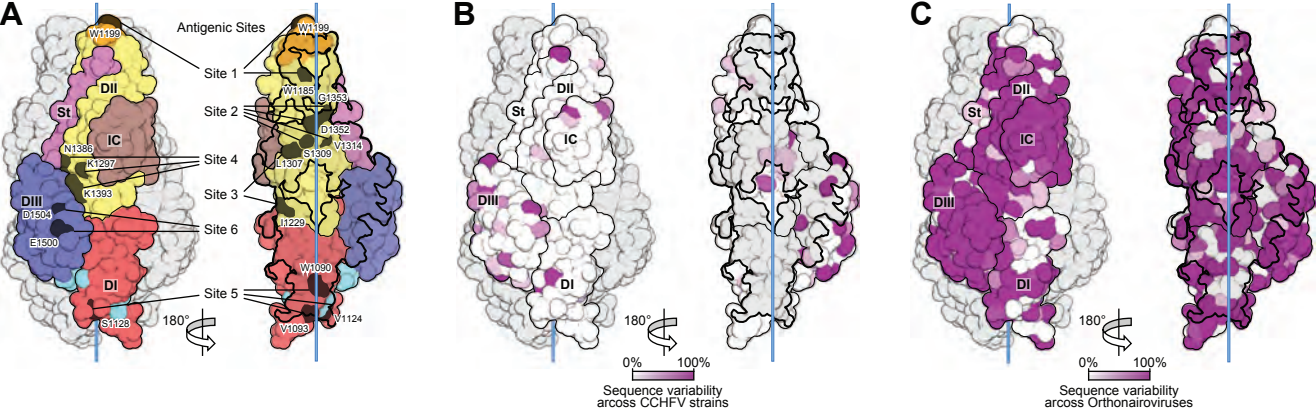
A
Antigenic Sites
Site 1
Site 2
Site 4
Site 3
Site 6
Site 5
W1199
DII
St
IC
N1386
K1297
K1393
DIII
D1504
E1500
DI
S1128
180°
W1199
W1185
G1353
D1352
V1314
S1309
L1307
I1229
W1090
V1124
V1093
B
DII
St
IC
DIII
DI
180°
0%
100%
Sequence variability
arcoss CCHFV strains
C
DII
St
IC
DIII
DI
180°
0%
100%
Sequence variability
arcoss Orthonairoviruses

Science
AAAS

Supplementary Materials for

Structural basis of synergistic neutralization of Crimean-Congo hemorrhagic fever virus by human antibodies

Akaash K. Mishra[1†], Jan Hellert[2‡†], Natalia Freitas[3], Pablo Guardado-Calvo[2], Ahmed Haouz[4], J. Maximilian Fels[5], Daniel P. Maurer[6], Dafna M. Abelson[7], Zachary A. Bornholdt[7], Laura M. Walker[6], Kartik Chandran[5], François-Loïc Cosset[3], Jason S. McLellan[1*], Felix A. Rey[2*]

Correspondence to: jmclellan@austin.utexas.edu; felix.rey@pasteur.fr

This PDF file includes:

Materials and Methods

Recombinant protein production

Mature CCHFV Gc, generated by processing of the polyprotein precursor by the host protease SKI-1 (*37*), spans codons 1041 to 1684 at the end of the single open reading frame of genomic segment M (Fig. 1A). The sequences used for our structural studies correspond to the IbAr10200 strain of CCHFV (GenBank: AF467768; UNIPROT: Q8JSZ3). To obtain soluble forms for structural studies we truncated Gc upstream of the trans-membrane (TM) segment, which spans residues 1595–1615. We made three different Gc constructs ending at residues 1579, 1572 and 1561, which also omits a putative amphipathic membrane-proximal external region immediately upstream of the TM segment. These constructs, respectively termed Gc^{1579}, Gc^{1572} and Gc^{1561}, were monomeric in solution, yet failed to yield diffraction-quality crystals. To prevent micro-aggregation of potential post-fusion trimers formed in solution, we introduced three-point mutations to replace aromatic residues exposed in the predicted fusion loop: W1191H, W1199A and W1197A to make the "Gc^{1561} W3" and "Gc^{1572} W3" mutant constructs. A similar strategy had been used in the past to obtain crystals of other class II fusion proteins in the post-fusion form (*17, 38*). The recombinant CCHFV Gc W3 mutants eluted as two distinct peaks in size-exclusion chromatography (SEC), corresponding to trimer and monomer, whereas no soluble trimer was detected for the wild-type counterpart (Fig. S2).

Crystals of the post-fusion trimer were obtained using recombinant protein produced in *Drosophila* S2 cells (Thermo Fisher Scientific Cat# R690-07) stably transfected with the pMT expression vector (Invitrogen) expressing synthetic, codon-optimized genes (Invitrogen) starting with the *Drosophila* BiP signal sequence for efficient secretion into the culture medium. The Gc^{1561} wild-type and W3 mutant constructs carried at their C-termini the sequence ENLYFQSAG **WSHPQFEK** GGGSGGGSGGGS **WSHPQFEK** containing a Twin-Strep-tag (in bold) and a TEV protease cleavage site (underlined). The Gc^{1572} W3 wild-type and mutant

constructs had a single Strep tag (sequence: **WSHPQFEK**) fused to their N-termini, immediately after the signal sequence.

Adherent S2 cell cultures were grown in Insect-XPRESS protein-free medium with L-glutamine (Lonza) supplemented with 25 U/mL penicillin/streptomycin (Gibco) at 28°C. Expression plasmids were co-transfected with the selection plasmid pCoPURO (*39*) at a mass ratio of 20:1 using the Effectene transfection reagent (Qiagen) according to the manufacturer's instructions. Polyclonal stable S2 cell lines were established by selection with 7.5 µg/mL puromycin (*Invivogen*), which was added to the medium 40 h after transfection. Cultures were expanded to 1 L of 10^7 cells/mL in Erlenmeyer flasks shaking at 100 rpm at 28°C. Recombinant protein expression was subsequently induced with 5 µM $CdCl_2$. Cell supernatants were harvested one week after induction, concentrated to 50 mL on a 10 kDa MWCO PES membrane (Sartorius), pH-adjusted with 0.1 M Tris-HCl pH 8.0, cleared from biotin with 15 µg/mL avidin, cleared from precipitate by centrifugation at 4000 x g for 15 min at 8°C, and used for affinity purification on a 5 mL Strep-Tactin Superflow hc column (iba Life Science). Trimeric fractions were further purified by size exclusion chromatography (SEC) on a HiLoad Superdex 200 pg column (GE Healthcare) in 20 mM Tris-HCl pH 8.0, 150 mM NaCl. Protein concentrations were adjusted in 10 kDa MWCO PES Vivaspin centrifugal concentrators (Sartorius).

In order to remove the Twin-Strep-tag of the Gc^{1561} construct, the protein concentration was adjusted to 1 mg/mL for cleavage with 100 ng/mL trypsin (Sigma-Aldrich) for 60 min at 24°C. The reaction was stopped with 200 ng/mL soybean trypsin inhibitor (Sigma-Aldrich) and the cleavage products were separated by SEC in 20 mM Tris-HCl pH 8.0, 150 mM NaCl. The final sample was concentrated to 12 mg/mL in a 10 kDa MWCO PES Vivaspin centrifugal concentrator (Sartorius). The resulting crystal structure shows that trypsin cleaved the recombinant protein at the C-terminal end of its first Strep tag. We initially used TEV protease to remove the complete purification tag, but the resulting crystals were only of poor quality. Inspection of the crystal packing of the trypsin-cleaved protein indicated an involvement of the

TEV cleavage sequence and of the first Strep tag in inter-trimer contacts, explaining the difference in crystal quality between the two samples.

Gc^{1579}, which we used for co-crystallization with the two Fab fragments, was made from a construct containing residues 1–515 (including the authentic signal peptide of the precursor polyprotein) fused to 1041–1579 of the CCHFV poly-glycoprotein precursor with a furin cleavage site (RSKR) inserted in between the two segments. This construct was codon optimized for human cell expression (via GenScript) and cloned into a pαH eukaryotic expression plasmid with a C-terminal HRV3C protease cleavage site, an 8×HisTag, and a Twin-Strep-tag. The plasmid was transiently transfected into FreeStyle 293 cells (ThermoFisher Scientific Cat# R7007) using polyethyleneimine. Transfected FreeStyle 293 cells were treated with 5 μM kifunensine to ensure uniform high-mannose glycosylation. Cleavage with endogenous furin generated soluble monomeric Gc^{1579} which was secreted into the medium, harvested and purified over Strep-Tactin resin (IBA Lifesciences). After elution of Gc^{1579} from Strep-Tactin resin, the affinity tags were removed by HRV3C cleavage. Gc^{1579} was further purified by SEC using a HiLoad 16/600 Superdex 200 pg (GE Healthcare Biosciences) in 2 mM Tris-HCl (pH 8.0), 200 mM NaCl, and 0.02% NaN_3.

The light and heavy chain variable regions of human antibodies ADI-37801 and ADI-36121 were cloned into human Igκ and Igγ1 vectors, respectively. The Igγ1 vector contains a HRV3C protease site in the hinge region of the heavy chain. Plasmids encoding antibody heavy and light chains for ADI-37801 and ADI-36121 were co-transfected into FreeStyle 293-F cells. All IgG antibodies were eluted off the Protein A column using 0.1 M glycine pH 3.0 into a buffered solution containing 1/10 (*v/v*) of 1 M Tris-HCl pH 8.0. To produce ADI-37801 and ADI-36121 Fabs, corresponding IgGs were digested with HRV3C for 2 hours at room temperature, followed by passing the solution over protein A resin to remove the Fc, and subsequently purified by SEC using a Superdex 200 column (GE).

For crystallization, Gc^{1579} was mixed with a 2-fold molar excess of each Fab (ADI-37801 and ADI-36121) and the resulting complex was purified by SEC using a HiLoad 16/600 Superdex 200 pg (GE Healthcare Biosciences) in 2 mM Tris-HCl (pH 8.0), 200 mM NaCl, and 0.02% NaN_3.

Crystallization

Initial crystal screening with the trimeric Gc constructs was performed at the macromolecular crystallization platform of the Institut Pasteur (*40*). Optimal crystals of the trypsin-cleaved Gc^{1561} W3 trimer were obtained by the hanging-drop vapor diffusion method: 0.75 µL of 12 mg/mL protein in 20 mM Tris-HCl pH 8.0 and 150 mM NaCl were added to 0.50 µL of reservoir solution containing 0.1 M MES pH 6.5, 0.1 M $MgCl_2$ and 30% (v/v) PEG 400. The drops were equilibrated against reservoir solution on siliconized glass slides (Hampton) for 5 days at 18°C before crystals were conserved in liquid nitrogen without additional cryo-protection. Iodide derivate samples for SAD phasing were prepared by incubating native crystals in a drop containing 0.6 M NaI, 85 mM MES pH 6.5, 85 mM $MgCl_2$ and 26% (v/v) PEG 400 for 24 h before cryo-cooling without back-soaking.

Optimal crystals of the Gc^{1572} W3 trimer were obtained by the hanging-drop vapor diffusion method: 0.5 µL of 13.4 mg/mL protein in 20 mM Tris-HCl pH 8.0, 150 mM NaCl were added to 0.5 µL of reservoir solution containing 0.1 M HEPES pH 7.5, 10% (w/v) PEG 8K, 8% (v/v) ethylene glycol. The drops were equilibrated against reservoir solution one week at 18°C. Crystals were cryo-protected in 20% (v/v) glycerol, 80 mM HEPES pH 7.5, 8% (w/v) PEG 8K, 6.4% (v/v) ethylene glycol prior to conservation in liquid nitrogen.

Crystals of the ADI-36121 Fab in space group $P\ 2_1\ 2_1\ 2_1$ diffracting to 2.6 Å were obtained by the sitting-drop vapor diffusion method after mixing 100 nL of the Fab (12.6 mg/mL) to 50 nL of reservoir solution containing 0.1 M $MgCl_2$, 0.1 M $CaCl_2$, 0.1 M KNa Tartrate, 25% PEG 4K, 4% isopropanol, 0.1 M Bis-Tris-HCl pH 6.5.

Crystallization trials for the Gc^{1579}–ADI-37801–ADI-36121 complex were set up using the sitting-drop vapor diffusion method. The best diffracting crystals were grown in a solution of 0.1 M sodium citrate (pH 5.6), 2% methyl-pentane-diol, 13.4% PEG 8000 via hanging-drop vapor diffusion by mixing 1 µl of the ternary complex (5 mg/mL) with 1 µl of reservoir solution. Crystals were soaked in reservoir solution supplemented with 20% (v/v) glycerol as a cryoprotectant before being plunge frozen with liquid nitrogen.

X-ray data collection and structure determination

Native high-resolution X-ray diffraction data for CCHFV Gc^{1561} W3 were recorded on beamline ID23-1 at the ESRF in Grenoble, France, with a Pilatus 6M detector. The dataset was processed with XDS (*41*) and AIMLESS (*42*). For SAD phasing, two iodide derivate datasets of 360° (oscillation angle: 0.1°) were collected from a single crystal at a photon energy of 7 keV at beamline PX2 of synchrotron SOLEIL in St Aubin, France with an EIGER X 9M detector. The two derivate datasets were auto-processed with XDSME and merged with XSCALE (*41*). Significant anomalous signal reached to a resolution of 3.4 Å, and SAD phasing was carried out with PHENIX.AUTOSOL (*43*). The initial density map was readily interpretable through iterative cycles of manual model building in COOT (*44*) and automatic refinement in PHENIX.REFINE (*45*). Phases were extended to the high-resolution native dataset in PHENIX.MR (*45*).

X-ray diffraction data for CCHFV Gc^{1572} W3 were recorded on beamline PX2 at the SOLEIL synchrotron with an EIGER X 9M detector. The dataset was processed with XDS (*41*) and AIMLESS (*42*), and the structure was determined by molecular replacement with the CCHFV Gc^{1561} W3 model using PHENIX.MR (*45*).

X-ray diffraction data for the free ADI-36121 Fab and the Gc^{1579}–ADI-37801–ADI-36121 complex were collected at the 19-ID beamline (Advanced Photon Source; Argonne National Laboratories) and were processed using the CCP4 software suite *(46)*, indexed and integrated in iMOSFLM (*47*), and scaled and merged with AIMLESS *(42)*. A molecular

replacement solution for the ADI-36121 Fab dataset was found by PHASER *(48)* using a chimeric protein model consisting of the heavy and light chains of PDB ID: 5I19 and PDB ID: 1HEZ, respectively, separated into the constant and variable domains as search models. The ADI-36121 Fab structure was built in COOT (*44*) and refined using PHENIX *(45)* to an R_{work} / R_{free} of 19.9 % / 24.1 %. This structure was then used to find a molecular replacement solution for ADI-36121 and ADI-37801 Fabs in the structure of Gc and Fab complex. The initial structure of Gc^{1579} was built using ARP/wARP *(49, 50)* by manually placing orthohantavirus Gc structure (PDB ID: 5J9H) that had been processed in Sculptor *(51)* with default settings. The structure of Gc and the Fab complex was finally built manually in COOT *(44)* as a part of iterative model building and refined using PHENIX *(45)* to an R_{work}/R_{free} of 21.9 % / 24.4 %. The structure was displayed using PYMOL (DeLano WL. The PyMOL Molecular Graphics System. Schrödinger LLC. 2002; Available: http://www.pymol.org). All crystallographic statistics are summarized in Table S1.

Multi-angle static light scattering

Purified recombinant proteins at concentrations of 1 mg/mL were subjected to SEC on a Superdex 200 10/300 column (GE Healthcare) equilibrated in 20 mM Tris-HCl, 150 mM NaCl, pH 8.0. Elutions were performed at 20 °C with a flow rate of 0.5 mL/min. Online multi-angle static light scattering analysis was performed with a DAWN-HELEOS II detector (Wyatt Technology). Online differential refractive index measurements were performed with an Optilab T-rEX detector (Wyatt Technology). Data were analyzed using the ASTRA software (Wyatt Technology).

Biolayer interferometry

IgG binding properties were determined using the OctetRed^{TM} system (ForteBio, Pall LLC). IgG was immobilized on anti-hIgG (AHC) sensors (FortéBio cat#18-5060) in 1x kinetics buffer (10 mM HEPES, 150 mM NaCl, 3 mM EDTA, 1 mg/mL bovine serum albumin [BSA], and 0.05% Tween 20 [pH 7.5]) in 96-half well black flat bottom polypropylene microplates

(FortéBio cat#3694). For the low pH experiments HEPES was replaced with Sodium Citrate to attain a final pH of 5.5, keeping all other constituents the same. Association and dissociation curves were measured for IgG binding to Gc. An antibody-captured AHC sensor was also dipped in a well containing kinetics buffer (with no binding protein) to allow single-reference subtraction to compensate for the slow dissociation of the antibody from the sensors. The data analysis was performed using the FortéBio Data Analysis 8.1 software and fitted to a 1:1 binding model to determine K_D, k_{on}, and k_{off}. All affinity measurement experiments were performed in duplicates.

Cell-cell fusion assay

Huh7 (RRID:CVCL_0336) "donor" cells ($2x10^5$ cells seeded 24 h before transfection) were co-transfected with 3 μg of pCAGGS-GP plasmid (*52, 53*) encoding the CCHFV poly-glycoprotein precursor, either wild type or carrying a single amino acid mutation within the Gc moiety and 100 ng of an HIV-1 long terminal repeat (LTR)-luciferase reporter plasmid (a kind gift of Françoise Bex, Institut de Recherches Microbiologiques Jean-Marie Wiame, Belgium). For a negative control, cells were co-transfected with 3 μg of empty phCMV plasmid and 100 ng of the HIV-1-LTR-luciferase reporter plasmid. Huh7 "indicator" cells were transfected with the expression vector LXSN-Tat encoding for HIV-1 Tat (*54*). Huh7 donor and indicator cells were transfected with GeneJammer transfection reagent (Agilent) following the manufacturer´s instructions. The next day, the transfected cells were detached with Versene (0.53 mM EDTA; Invitrogen), counted, and reseeded at a 1:3 donor to indicator cells ratio and co-cultivated overnight in DMEM media supplemented with 10% FCS. Then, the co-cultures were washed with PBS, incubated for 3 min in fusion buffer (130 mM NaCl, 15 mM sodium citrate, 10 mM MES [morpholineethanesulfonic acid], 5 mM HEPES) at either pH 4 or pH 7 at room temperature. Following acidic or neutral pH treatment co-cultures were washed twice with pre-warmed DMEM media with 10% FCS and incubated for an additional period of 16-24 hours before being lysed with 1x passive lysis buffer (Promega) and luciferase luminescence

measured using a luminescence reader with integrated injectors after automatic addition of firefly luciferase reagent. Luciferase signals were normalized by the background signal of a mock-transfected control. All data are represented as means ± standard deviation of 6 to 16 replicates per condition, and they were analyzed using the Mann-Whitney test: ns, not significant ($P > 0.05$); **, $P < 0.01$; ***, $P < 0.001$; and ****, $P < 0.0001$).

Cell surface expression of CCHFV Gc wild type and mutants was confirmed by FACS 48 h after transfection (of 293T cells, RRID:CVCL_0063) using the anti-Gc murine antibody 11E7 (BEI Resourses NR-40277; (*55*)) and a goat anti-mouse IgG secondary antibody conjugated with APC.

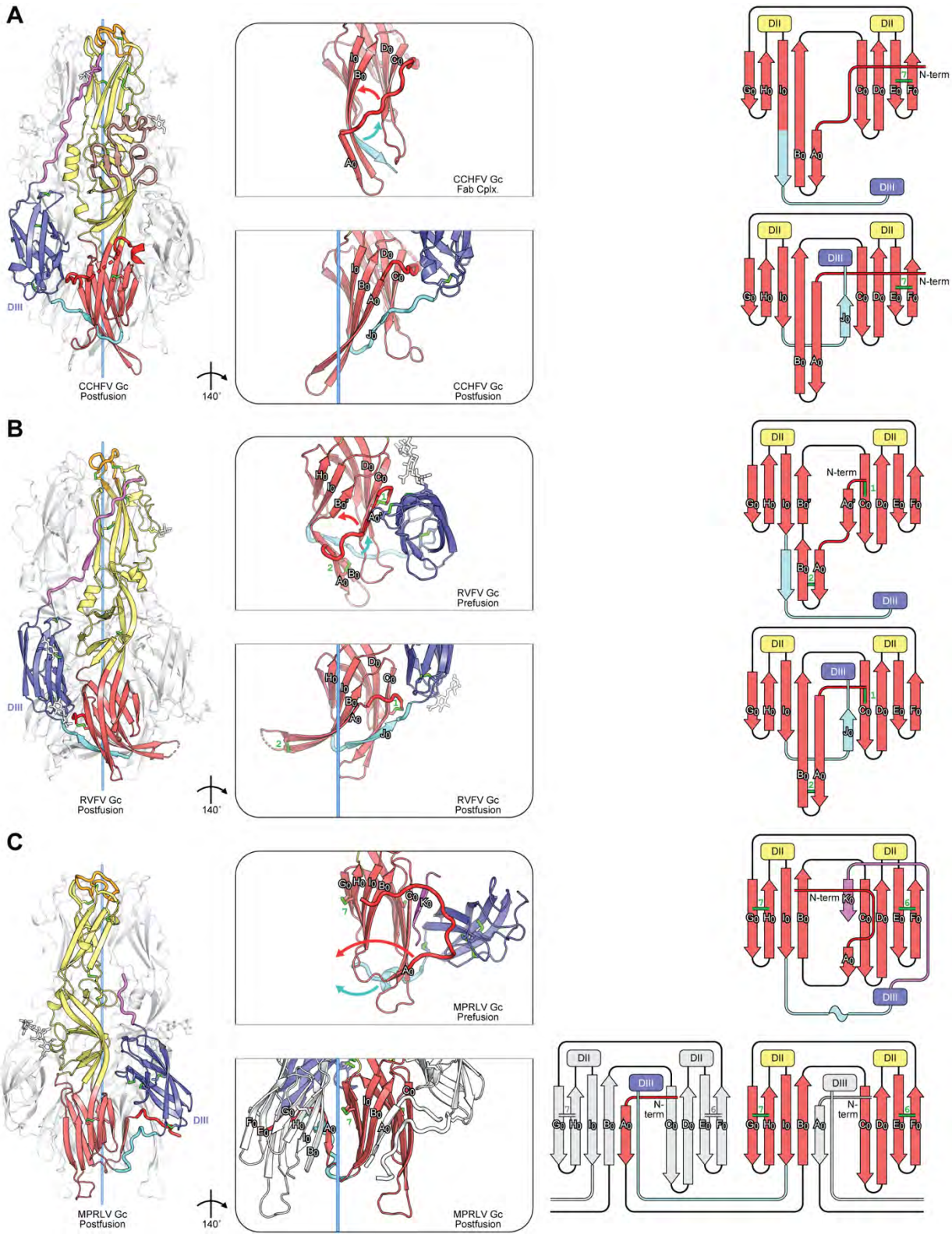

Fig. S1.

Conformational changes in bunyavirus Gc domain I. A, B and C: Left column, the X-ray structures of the post-fusion Gc trimer for bunyaviruses belonging to three different families, as indicated. Note the domain III swap in the trimer of the bottom panel (which goes to the

right) compared to the upper two panels, in which domain III goes to the left (for clarity, only the front subunit of each trimer is colored according to domains as in Fig. 1). Middle column, comparison of domain I in pre- (top) and post-fusion (bottom) forms, rotated as indicated from the view of the left panel. Right panel**,** topology diagrams of domain I in pre-fusion (top) and post-fusion (bottom) form: **A)** CCHFV (*Nairoviridae* family) **B)** RVFV (*Phenuiviridae* family) (top, PDB:4hj1 (*25*), bottom PDB:6egu (*17*)) **C)** MPRLV (*Hantaviridae* family) (top, PDB:6y62; bottom, PDB:6y68 (*26*)). For the latter, fragments of neighboring protomers in the post-fusion trimer are shown in grey. The trimer axis is shown in light blue in the left and middle panels. Curved colored arrows in the middle panels indicate the rearrangements converting the putative pre-fusion structure into the post-fusion hairpin. It is not known if the domain III swap in the post-fusion trimer in arboviruses with respect to non-arboviruses is a coincidence or if it has an underlying significance.

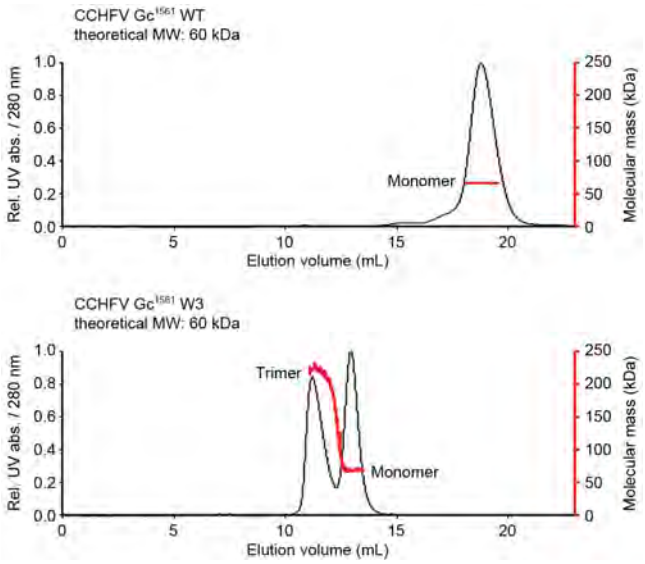

Fig. S2. Soluble fractions of the CCHFV Gc^{1561} wild-type and Gc^{1561} W3 mutant. Samples were eluted from a Superdex 200 10/300 SEC column (GE Healthcare) in 20 mM Tris-HCl, 150 mM NaCl, pH 8.0. The molecular mass in solution was determined by multi-angle static light scattering (MALS). The unusually high elution volume for the wild-type monomer suggests that the protein was held back by weak attractive interactions between its fusion loops and the column matrix. A similar behavior has been observed with monomeric class II fusion proteins (i.e, with the fusion loops exposed) from other viruses (e.g. alphaviruses (*56*)).

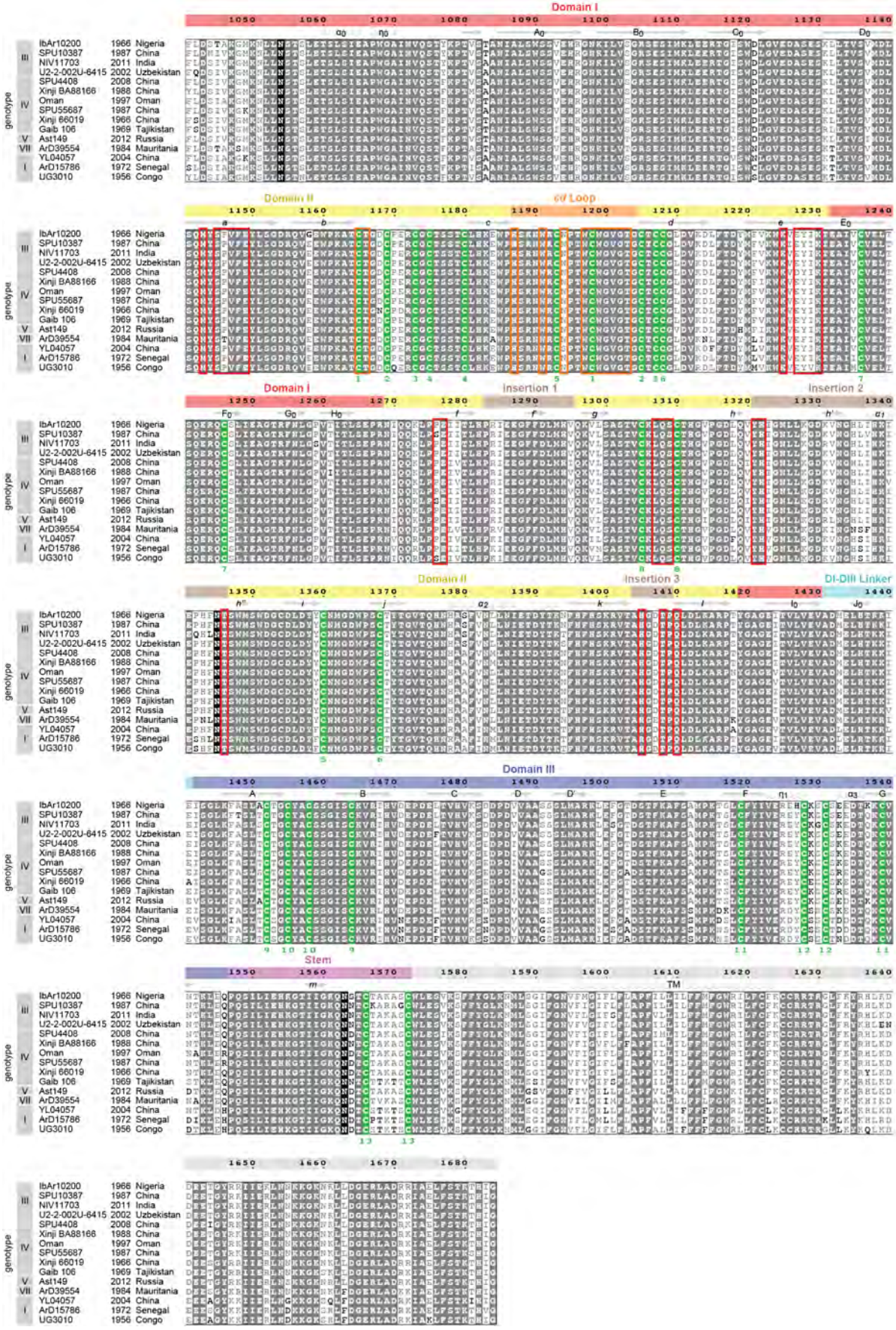
Domain I
Domain II
60 Loop
Domain I
Insertion 1
Insertion 2
Domain II
Insertion 3
DI-DIII Linker
Domain III
Stem
TM
genotype
III
IV
V
VII
I
IbAr10200 1966 Nigeria
SPU10387 1987 China
NIV11703 2011 India
U2-2-002U-6415 2002 Uzbekistan
SPU4408 2008 China
Xinji BA88166 1988 China
Oman 1997 Oman
SPU55687 1987 China
Xinji 66019 1966 China
Gaib 106 1969 Tajikistan
Ast149 2012 Russia
ArD39554 1984 Mauritania
YL04057 2004 China
ArD15786 1972 Senegal
UG3010 1956 Congo

Fig. S3. Conservation of Gc across CCHFV strains. Gc sequence alignment across 15 representative CCHFV strains. Identical residues in the alignment are highlighted with grey background and highly divergent residues are shown in black font. The ADI-37801 epitope is boxed in orange and the ADI-36121 epitope is boxed in red. Disulfides are highlighted with green background and are labelled. N-glycosylation sites are highlighted with black background. CCHFV Gc contains three N-linked glycosylation sites, at Asn1054, Asn1345 and Asn1563 (Fig. 1C-D). The first one lies within a mobile segment that is disordered in the crystals. The Asn1345 glycan lies within a cluster of orthonairovirus-specific sequence insertions at the domain II base (insertion cluster (IC), brown in Fig. 1C-D), from which it projects laterally. The Asn1563 glycan lies approximately 20 Å away from the HMIS (Fig. 1C), in a location where the sugar chain would be within reach of the merging membranes during fusion. However, this glycan does not serve a critical function, as it is not essential for membrane fusion (Fig. 2D) and was found to be dispensable for virus growth (*28*).

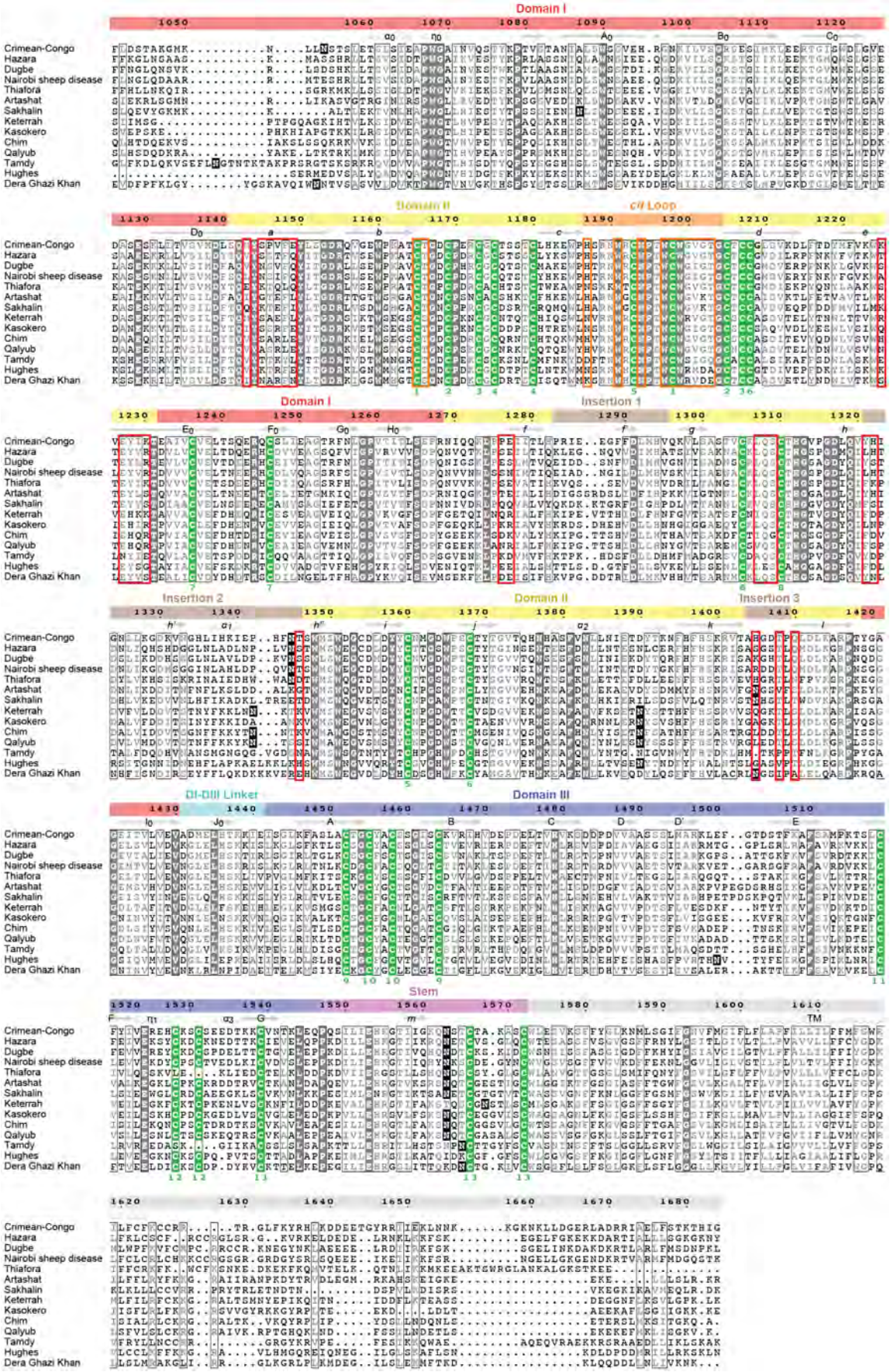
Domain I
Domain II
β-barrel Loop
Domain I
Insertion 1
Insertion 2
Domain II
Insertion 3
DI-DIII Linker
Domain III
Stem
TM
Crimean-Congo
Hazara
Dugbe
Nairobi sheep disease
Thiafora
Artashat
Sakhalin
Keterrah
Kasokero
Chim
Qalyub
Tamdy
Hughes
Dera Ghazi Khan

Fig. S4. Conservation of Gc across the *Orthonairovirus* genus. Gc sequence alignment across 14 species of the Orthonairovirus genus. Disulfides are highlighted with green background and are labelled. N-glycosylation sites are highlighted with black background. Identical residues in the alignment are highlighted with grey background and highly divergent residues are shown in black font. The ADI-37801 epitope is boxed in orange and the ADI-36121 epitope is boxed in red.

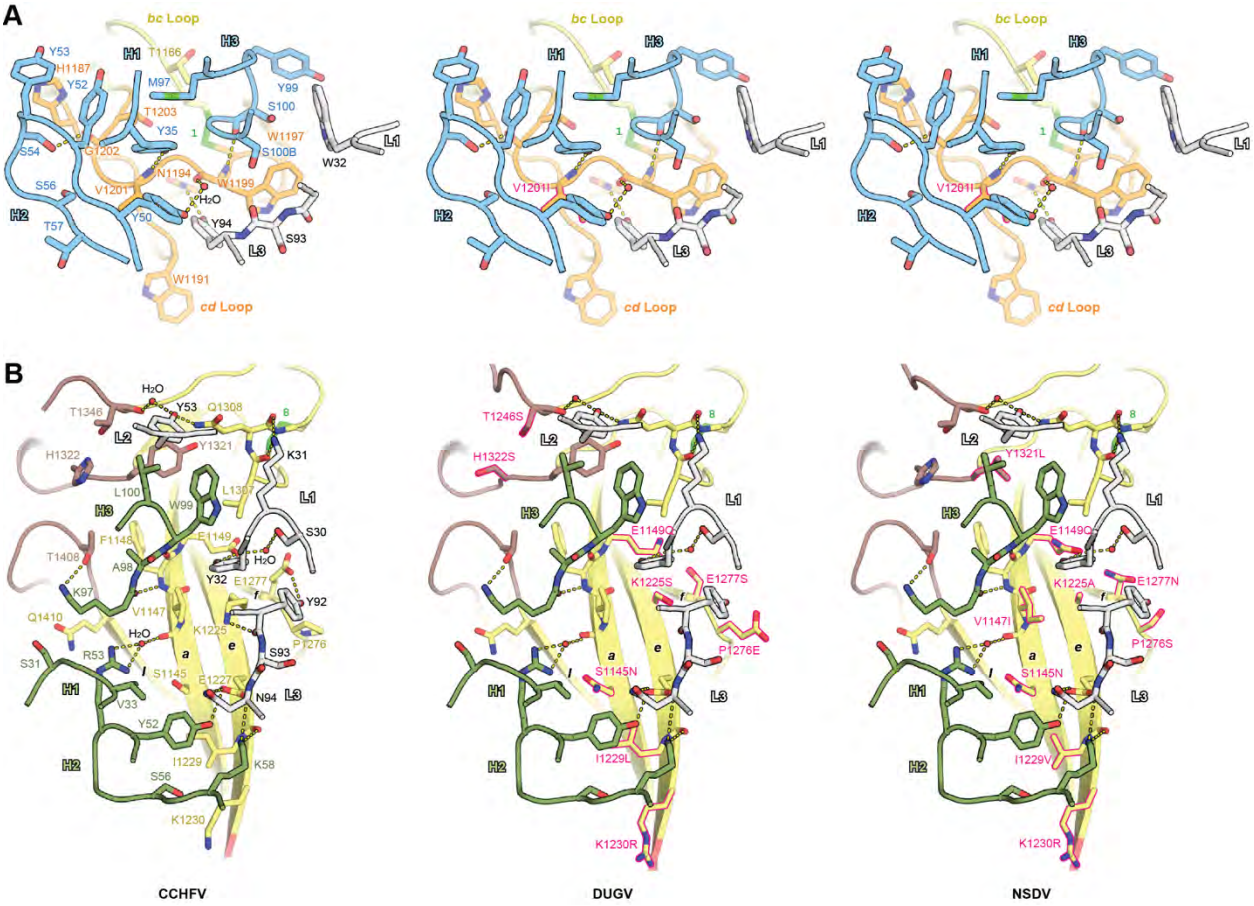

Fig. S5. Epitope deviations in Dugbe virus (DUGV) and Nairobi sheep disease virus (NSDV). A) The paratope of ADI-37801 in complex with the epitope of CCHFV (left) compared to homology models of the respective complexes for DUGV (center) and NSDV (right). The view corresponds to Fig. 2F. **B)** The paratope of ADI-36121 in complex with the epitope of CCHFV (left) compared to homology models of the respective complexes for DUGV (center) and NSDV (right). The view corresponds to Fig. 3B. Amino acid changes are highlighted in magenta for DUGV and NSDV. The homology models were prepared with the Swiss-Model server (*57*).

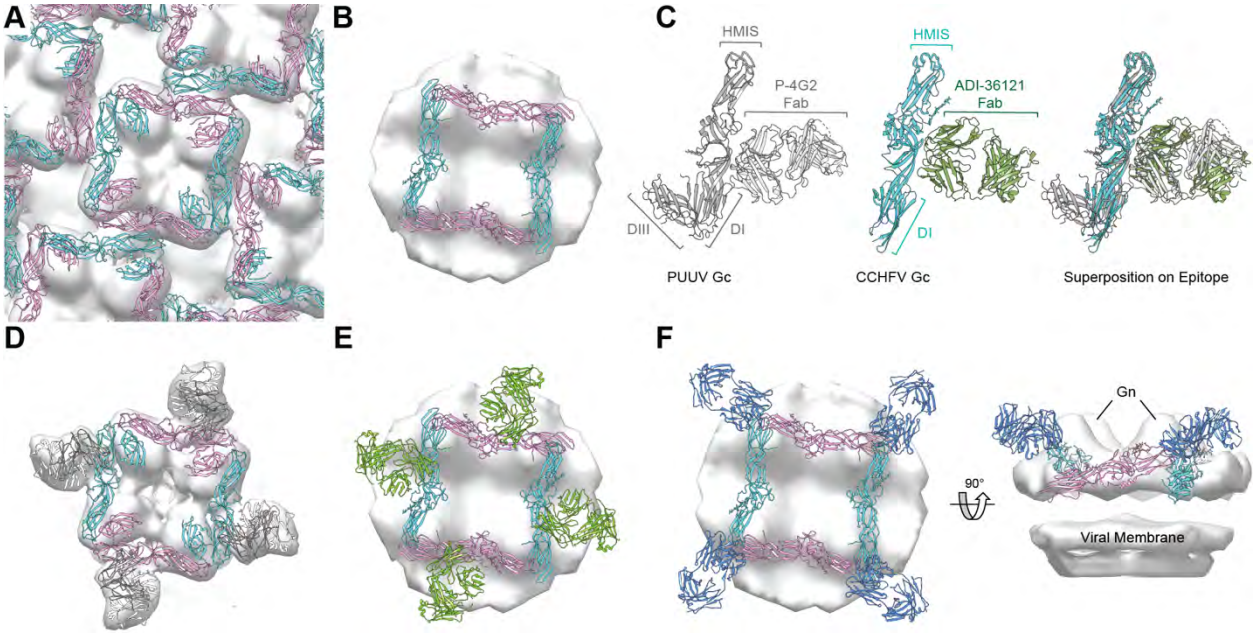

Fig. S6. ADI-36121 targets a similar site of vulnerability as observed for hantavirus Gc. **A)** Puumala virus (PUUV) pre-fusion Gc fitted into the hantavirus surface lattice derived from cryo-electron tomography (cryo-ET) (PDB:7b0a, EMD-11966) (*36*). Adjacent Gc monomers are colored in pink and cyan. **B)** CCHFV Gc monomer fitted into the nairovirus surface lattice derived from cryo-ET (*34*). Adjacent Gc monomers are colored in pink and cyan. **C)** Left: P-4G2 Fab bound to PUUV Gc (*36*) (PDB:6z06, grey), middle: Fab ADI-36121 (green) bound to CCHFV Gc (cyan), right: superposition of the two structures on the epitope. The superposition is on 23 alpha carbons of *a* and *e* strands with an RMSD of 1.4 Å. CCHFV Gc and PUUV Gc share an overall sequence identity of only 17%, yet the two structures have an RMSD of 3.6 Å over 411 residues. **D)** PUUV Gc bound to P-4G2 Fab (*36*) fitted into the respective cryo-ET map of the Fab-bound spike (PDB:7b09, EMD-11964). **E)** CCHFV Gc bound to ADI-36121 Fab fitted into cryo-ET map of nairovirus spike. **F)** CCHFV Gc bound to ADI-37801 Fab fitted into cryo-ET map of the nairovirus spike displayed as top view (left) and side view (right).

Table S1.

Crystallographic data collection and refinement statistics.

	Gc^{1561} W3 trimer	**Gc^{1572} W3 trimer**	**Gc^{1579} Fabs complex**	**ADI-36121 Fab**
PDB ID	7A59	7A5A	7L7R	7KX4
Reservoir solution for crystallization	0.1 M MES pH 6.5 0.1 M $MgCl_2$ 30% (v/v) PEG 400	0.1 M HEPES pH 7.5 10% (w/v) PEG 8K 8% (v/v) ethylene glycol	0.1 M sodium citrate pH 5.6 2% (v/v) MPD 13.4% (w/v) PEG 8K	0.1 M $MgCl_2$, 0.1 M $CaCl_2$ 0.1 M K/Na Tart 25% (w/v) PEG 4K 4% isopropanol 0.1 M Bis-Tris-HCl pH 6.5
Data collection				
Space group	$C\,2\,2\,2_1$	$P\,1\,2_1\,1$	$P\,2_1\,2_1\,2_1$	$P\,2_1\,2_1\,2_1$
Wavelength (Å)	1.044	0.980	0.979	0.979
Cell dimensions				
a, *b*, *c* (Å)	70.0, 216.1, 274.3	77.0, 108.3, 223.5	60.2, 95.2, 323.0	58.2, 76.6, 208.5
α, β, γ (°)	90, 90, 90	90, 93.22, 90	90, 90, 90	90, 90, 90
Resolution range (Å)	48.91-2.20 (2.28- 2.20)	49.05-3.00 (3.10-3.00)	43.1-2.1 (2.14-2.10)	51.5-2.6 (2.71-2.60)
R_{sym}	0.068 (1.053)	0.169 (1.203)	0.094 (1.134)	0.202 (0.796)
$\langle I/\sigma(I)\rangle$	16.8 (1.5)	8.7 (1.2)	9.5 (1.7)	8.1 (2.4)
$CC_{1/2}$	0.999 (0.725)	0.996 (0.588)	0.997 (0.697)	0.987 (0.736)
Completeness (%)	99.7 (97.8)	99.3 (93.5)	98.5 (99.8)	100 (100)
Redundancy	7.1 (7.3)	7.0 (6.5)	6.1 (6.2)	6.9 (5.7)
Total reflections	754,138 (74,882)	520,158 (44,674)	656,856 (33,169)	206,107 (20,408)
Unique reflections	105,819 (10,254)	73,899 (6,924)	107,701 (5,342)	29,766 (3,571)
Refinement				
Resolution range (Å)	48.91-2.20 (2.28- 2.20)	49.05-3.00 (3.10-3.00)	43.1-2.1 (2.14-2.10)	51.5-2.6 (2.69-2.60)
Unique reflections	105,807 (10,253)	73,878 (6,912)	107,532 (3624)	29,696 (2659)
R_{work} / R_{free} (%)	16.1/19.4 (29.3/32.5)	20.4/24.0 (34.6/36.9)	21.9/24.4 (32.9/36.2)	19.9/24.1 (26.4/32.6)
Number of atoms	12,589	23,452	9,730	6,842
Protein	11,761	23,321	9,295	6,524
Water	729	0	396	318
Ligands	99	131	39	0
Average *B*-factor (Å^2)	72.77	93.95	67.1	36.5
Protein	73.0	93.63	67.7	36.8
Water	62.4	-	54.1	30.4
Ligands	126.4	152.28	54.1	-
R.m.s. deviations				
Bond lengths (Å)	0.006	0.004	0.006	0.006
Bond angles (°)	0.81	0.59	0.815	0.892
Ramachandran (%)				
Favored	97.2	97.3	97.0	98.3
Allowed	2.7	2.6	3.0	1.7
Outliers	0.1	0.2	0.0	0.0

Data in parentheses are for the highest resolution shell.

Table S2.

Epitope Details

Residue	Position	Buried surface area (Å^2)	Polar interactions with antibody
ADI-37801			
C1165	*bc* loop	14.8	-
T1166	*bc* loop	52.7	-
H1187	*cd* loop	68.6	-
W1191	*cd* loop	34.5	-
N1194	*cd* loop	3.9	Hydrogen bond to $Y94_{LC}$
W1197	*cd* loop	36.3	-
C1198	*cd* loop	4.0	-
W1199	*cd* loop	172.7	Hydrogen bond to $S100_{HC}$
G1200	*cd* loop	8.7	-
V1201	*cd* loop	117.1	Hydrogen bond to $Y35_{HC}$
G1202	*cd* loop	33.6	Hydrogen bond to $S54_{HC}$
T1203	*cd* loop	49.1	-
ADI-36121			
M1143	β-strand *a*	5.9	-
S1145	β-strand *a*	35.4	-
P1146	β-strand *a*	21.7	-
V1147	β-strand *a*	53.5	-
F1148	β-strand *a*	31.0	Hydrogen bonds to $K97_{HC}$ and $W99_{HC}$
E1149	β-strand *a*	18.0	Hydrogen bond to $Y32_{LC}$
K1225	β-strand *e*	77.6	Hydrogen bond to $Y92_{LC}$
E1227	β-strand *e*	82.9	Hydrogen bonds to $Y52_{HC}$, $K58_{HC}$ and $N94_{LC}$, salt bridge to $K58_{HC}$
Y1228	β-strand *e*	5.2	Hydrogen bond to $K58_{HC}$
I1229	β-strand *e*	75.3	-
K1230	β-strand *e*	17.4	-
P1276	H_0*f* loop	17.0	-
E1277	β-strand *f*	20.1	Hydrogen bond to $Y92_{LC}$
L1307	*gh* loop	92.8	Hydrogen bond to $K31_{LC}$
Q1308	*gh* loop	60.6	Hydrogen bond to $Y53_{LC}$
S1309	*gh* loop	7.9	-
Y1321	*hh'* loop	33.4	-
H1322	*hh'* loop	19.3	-
T1346	*h'h''* loop	20.1	-
H1405	*kl* loop	26.5	-
T1408	*kl* loop	44.2	Hydrogen bond to $K97_{HC}$
Q1410	β-strand *l*	75.0	Hydrogen bond to $R53_{HC}$